AGU PUBLICATIONS

Water Resources Research

RESEARCH ARTICLE
10.1002/2017WR021127

Key Points:
- A three-dimensional approach was employed to examine artificial mixing in a drinking-water reservoir
- Epilimnetic mixing resulted in three-dimensional heterogeneity in thermal structure in the water body
- Constituent transport between littoral and deep regions was enhanced during epilimnetic mixing

Supporting Information:
- Supporting Information S1

Correspondence to:
C. Lei,
chengwang.lei@sydney.edu.au

Citation:
Chen, S., Little, J. C., Carey, C. C., McClure, R. P., Lofton, M. E., & Lei, C. (2018). Three-dimensional effects of artificial mixing in a shallow drinking-water reservoir. *Water Resources Research*, *54*, 425–441. https://doi.org/10.1002/2017WR021127

Received 19 MAY 2017
Accepted 28 DEC 2017
Accepted article online 8 JAN 2018
Published online 25 JAN 2018

Three-Dimensional Effects of Artificial Mixing in a Shallow Drinking-Water Reservoir

Shengyang Chen[1], John C. Little[2], Cayelan C. Carey[3], Ryan P. McClure[3], Mary E. Lofton[3], and Chengwang Lei[1]

[1]School of Civil Engineering, University of Sydney, Sydney, NSW, Australia, [2]Department of Civil and Environmental Engineering, Durham Hall, Virginia Tech, Blacksburg, VA, USA, [3]Department of Biological Sciences, Derring Hall, Virginia Tech, Blacksburg, VA, USA

Abstract Studies that examine the effects of artificial mixing for water-quality mitigation in lakes and reservoirs often view a water column with a one-dimensional (1-D) perspective (e.g., homogenized epilimnetic and hypolimnetic layers). Artificial mixing in natural water bodies, however, is inherently three dimensional (3-D). Using a 3-D approach experimentally and numerically, the present study visualizes thermal structure and analyzes constituent transport under the influence of artificial mixing in a shallow drinking-water reservoir. The purpose is to improve the understanding of artificial mixing, which may help to better design and operate mixing systems. In this reservoir, a side-stream supersaturation (SSS) hypolimnetic oxygenation system and an epilimnetic bubble-plume mixing (EM) system were concurrently deployed in the deep region. The present study found that, while the mixing induced by the SSS system does not have a distinct 3-D effect on the thermal structure, epilimnetic mixing by the EM system causes 3-D heterogeneity. In the experiments, epilimnetic mixing deepened the lower metalimnetic boundary near the diffuser by about 1 m, with 55% reduction of the deepening rate at 120 m upstream of the diffuser. In a tracer study using a 3-D hydrodynamic model, the operational flow rate of the EM system is found to be an important short-term driver of constituent transport in the reservoir, whereas the duration of the EM system operation is the dominant long-term driver. The results suggest that artificial mixing substantially alters both 3-D thermal structure and constituent transport, and thus needs to be taken into account for reservoir management.

1. Introduction

Engineered systems that mix and/or oxygenate are increasingly deployed in lakes and reservoirs for water-quality management (e.g., Imteaz & Asaeda, 2000; Singleton & Little, 2006; Toffolon et al., 2013; Visser et al., 2016). Understanding the performance of oxygenation and mixing systems is crucial for successful design and operation to improve water quality and avoid adverse unintended outcomes (see Imteaz et al., 2009). Water bodies with strong stratification may develop anoxia due to microbial respiration and the lack of mixing across the thermocline. Anoxia in the hypolimnion stimulates internal nutrient loading due to the reduction of redox potential at the sediment-water interface, which may cause the release of phosphorus (Lake et al., 2007; Nürnberg et al., 1986). Studies have shown that, with proper design, oxygenation devices can replenish depleted dissolved oxygen (DO) in the hypolimnion (Gantzer et al., 2009; Gerling et al., 2014; Sherman et al., 2012; Wüest et al., 1992), which may help to suppress the release of ammonium, phosphorus, and reduced iron and manganese from the sediments (Davison, 1993; Gerling et al., 2014, 2016; Munger et al., 2016; Singleton & Little, 2006). On the other hand, mixing and destratification systems can be used to enhance vertical exchange of DO in water by reducing thermal stability and to keep the well-mixed water oxygenated (Fernandez et al., 2012).

In contrast, poorly operated oxygenation and mixing systems may give rise to detrimental effects, such as premature destratification and deterioration of water quality (Nürnberg et al., 2003; Toffolon et al., 2013). Thermal destratification caused by artificial mixing may increase nutrient transport causing surface algal blooms during summer stratified periods (Nürnberg et al., 2003). Artificial-mixing-induced destratification may also lead to reduction of DO in the hypolimnion owing to the lower DO saturation and the higher induced oxygen demand associated with warmer bottom water (Gerling et al., 2014). Among the recently studied oxygenation and mixing devices are side-stream supersaturation (SSS) hypolimnetic oxygenation

systems (Gerling et al., 2014), large-scale destratification aeration systems (Harris et al., 2015), and epilimnetic bubble-plume mixing (EM) systems (Chen et al., 2017).

When investigating the effects of artificial mixing in lakes and reservoirs, most studies adopted either one-dimensional (1-D) or two-dimensional (2-D) approaches to collect and analyze data from field experiments or numerical simulations (Becker et al., 2006; Heo & Kim, 2004; Imteaz et al., 2009; Singleton et al., 2013; Toffolon & Serafini, 2013). The vertical profiles of temperature and environmental constituents (e.g., DO) over water columns are usually the major focus, with horizontal homogeneity within individual water layers typically assumed (e.g., Heo & Kim, 2004; Imteaz et al., 2009). Thus, when it comes to hydrodynamic modeling of mixing in water bodies, 1-D or 2-D numerical models are commonly employed, including DYRESM (Imberger et al., 1978), GLM (Hipsey et al., 2013), and CE-QUAL-W2 (Cole & Wells, 2006; Singleton et al., 2013). Nevertheless, three-dimensional (3-D) hydrodynamic models may be more appropriate for investigating the mixing effects, because 3-D models can account for continuous horizontal and vertical variations of thermal structure and transport of constituents across the entire water body. Since oxygenation and mixing devices are usually deployed in discrete locations in reservoirs, adopting a 3-D approach for field experiments may elucidate heterogeneous mixing effects and fully account for potential interactions between the shallow and deep regions in the reservoir, especially for modeling unevenly distributed constituents in the water body.

Using in situ experiments and 3-D numerical simulations, the present study investigates thermal structure and constituent transport (of DO and turbidity) in a shallow drinking-water reservoir, in which both SSS and EM systems were deployed and operated. We were specifically interested in using the results from both field experiments and numerical simulation to analyze the effects of the SSS and EM operation in the reservoir. The mixing-induced interaction between the shallow and deep regions of the reservoir has the potential to substantially influence DO dynamics and pollutant transport, which may consequently affect water quality.

The present research analyzes, for the first time, the 3-D effects of heterogeneous mixing induced by concurrent operation of the two water-quality management devices, which were installed in the deep (lacustrine) region of the reservoir. Building on our earlier work (Chen et al., 2017), which focused on the effects of mixing and oxygenation in the deep region only, this study aims to identify the dominant 3-D characteristics of thermal structure and constituent transport across the reservoir during mixing using field and numerical data. Moreover, the present study highlights the importance of investigating the 3-D artificial mixing effects in both field experiments and numerical simulations.

2. Methodology

2.1. Experiment

The study site is Falling Creek Reservoir (FCR) in Vinton, Virginia, USA (37°18′12″N, 79°50′14″W), which is managed by the Western Virginia Water Authority (WVWA) for domestic water supply. The reservoir has a maximum water depth of 9.3 m with an average depth of 4 m and a volume of 3.1×10^5 m^3 at full pond. The reservoir is equipped with SSS and EM systems to control water quality during the stratified period. The SSS system is designed to increase DO in the hypolimnion and suppress the release of soluble iron, manganese, and phosphorus from the sediments, without destratifying the reservoir (Gerling et al., 2014). The EM system is designed to simultaneously mix and deepen the mixed layer, thereby disrupting the growth of some phytoplankton taxa (e.g., cyanobacteria) by decreasing their access to light and nutrients (e.g., Visser et al., 2016). The layout of the two systems is shown in Figure 1a.

The distribution header of the SSS system was deployed at ~1 m above the sediments in the hypolimnion while the diffuser of the EM system was located ~5 m below the water surface near the lower boundary of the metalimnion. Detailed descriptions of the SSS and EM systems are provided in previous studies (Chen et al., 2017; Gerling et al., 2014).

Field data were collected to illustrate the spatial and temporal variations of scalar properties across the whole reservoir. As shown in Figure 1a, we monitored both the longitudinal section and lateral transects in the reservoir. The longitudinal section extended from the upstream shallow region (FCR10) to the deep region (FCR50). Full water column profiles along the thalweg of FCR were collected, consisting of FCR10,

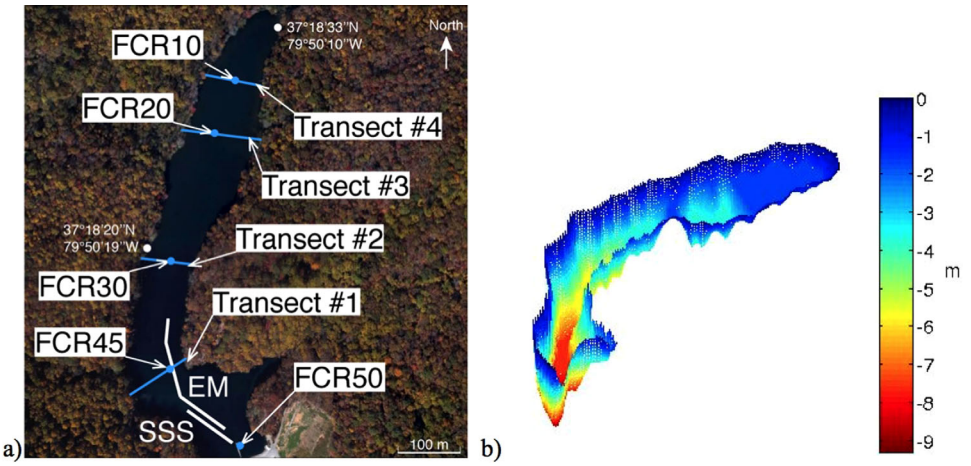

Figure 1. (a) Schematic diagram showing locations of EM diffuser, SSS distribution header, and the monitoring sites; (b) 3-D FCR bathymetry in Si3D.

FCR20, FCR30, FCR45, and FCR50 as shown in Figure 1a, where FCR50 was the deepest point of the entire reservoir. We monitored four transects laterally across the reservoir with ropes fixed across the water surface (Transect #1 through Transect #4 in Figure 1a). Each of the transects had nine evenly spaced monitoring points, resulting in 36 monitoring sites in total.

Experiments were carried out during the summer in 2016 from Day 146 to Day 208 (26 May 2016 to 27 July 2016) with three periods when the EM system was operated at varying flow rates and with successively increasing duration (see Tables 1 and 2). The three EM experiments, which were carried out intermittently in collaboration with the WVWA to reduce the potential of premature destratification of the drinking-water reservoir, are referred to as EM1, EM2, and EM3, respectively. The schedule of the EM experiments (Tables 1 and 2) was developed in consideration of the constraints of the drinking-water supply requirement and model-estimated outcomes (Chen et al., 2017) to preserve thermal stratification with a wide range of EM flow rates tested (198–425 liters per minute [LPM]), which enabled us to examine realistic management conditions in an operational drinking-water reservoir. The SSS system was operated continuously over the

Table 1
Experimental Schedules

DoY 2016	146–149	150	151–177	178–179	180–205	206–208	209
SSS	Water @ 197 LPM (O_2 @ 11.3 and then 7.1 LPM)					215 LPM (14.2 LPM)	
EM		ON		ON		ON ON	
		EM1[a]		EM2[b]		EM3[c]	

[a]EM1: Turned on at 708 liters per minute (LPM) equivalent to 25 standard cubic feet per minute (scfm) for 6 h. SSS oxygen delivery rate maintained at 11.3 LPM (0.4 scfm). [b]EM2: Turned on at 425 LPM (15 scfm) for the first 7 h and at 283 LPM (10 scfm) for the remaining 17 h. SSS oxygen delivery rate reduced from 11.3 LPM (0.4 scfm) to 7.1 LPM (0.25 scfm) from Day 161 to Day 206. [c]EM3: See Table 2.

Table 2
EM3 Detailed Experimental Schedule

DoY 2016	206	207	208
SSS	Water @ 197 LPM (O_2 @ 7.1 LPM and then 11.3 LPM)		215 LPM (14.2 LPM)
EM	ON		ON
	198 LPM for 5 h 708 LPM for 2 h	354 LPM for 25 h 708 LPM for 6.5 h	

entire summer, with different water flow rates and oxygen delivery rates. The adjustment of the SSS operational conditions (e.g., the oxygen delivery rate) during the experimental period was based on the DO saturation level in the hypolimnion, with the goal to maintain the required DO concentration.

Temperature, DO, and turbidity data were collected from the field experiment on an approximately bihourly basis in the beginning of each EM experimental period (EM1–EM3) and on a weekly basis outside the mixing experimental periods. An SBE 19plus high-resolution (4 Hz sampling rate) Conductivity, Temperature, and Depth (CTD) profiler with a SBE 43 DO probe (Seabird Electronics, Bellevue, WA, USA) was used for monitoring different sites of the reservoir, with data validation and alignment using a ProODO meter (YSI Inc., Yellow Springs, OH, USA). The data resolution measured by the CTD was at ~0.1 m increments along each water column from the water surface to the bottom. The field data were processed following the procedures described in (Gerling et al., 2014). Meteorological data were obtained from an in situ weather station deployed on the dam of FCR (Campbell Scientific Inc., UT, USA). The sampling frequency of the station was one record per minute. The quality of the data collected by the weather station was checked against meteorological data measured at Roanoke Airport (11.8 km away from FCR), which was downloaded from the National Climatic Data Center of the National Oceanic and Atmospheric Administration (www.ncdc.noaa.gov).

2.2. Simulation

2.2.1. Hydrodynamic Model and the Coupled Models

The Si3D hydrodynamic model, a semi-implicit 3-D computational fluid dynamics code, was adopted in this study. The code employs a finite-difference method for numerical solution of the Navier-Stokes equations (Rueda & Schladow, 2003; Rueda et al., 2007). The governing equations include continuity equation, momentum equations, and scalar transport equations, which can be found in (Smith, 2006). In the hydrodynamic model, the numerical grid was generated based on the FCR bathymetry, which is shown in Figure 1b. The locations of the SSS and EM systems in the model were the same as their corresponding locations in the field. The interactions of the flows induced by the two mixing devices with the bulk water were resolved by coupled water-jet and bubble-plume models, respectively, which quantify the local momentum induced by the oxygenation and mixing processes.

The coupled water-jet model calculates the small-scale jet flow within the much larger grid cells in the hydrodynamic model. Details about the coupled water-jet model and its validation were described in (Chen et al., 2017). A linear bubble-plume model was employed to simulate the flow induced by the EM system, which releases air bubbles from a linear diffuser within the metalimnion. The bubble-plume model estimates the depth of the maximum plume rise (DMPR) dynamically under the condition that the momentum of the plume at the DMPR is zero. The application and validation of the linear bubble-plume model were described by Singleton et al. (2007, 2010).

2.2.2. Model Initialization in Si3D

Model initialization is carried out in terms of temperature fields and other scalar fields (tracers). The temperature profile at FCR50, which is at the deepest end of the reservoir, is used to initialize the temperature scalar across the entire computational domain. The numerical model is then allowed to spin up for up to a week under the influence of the observed field weather conditions before each EM experiment.

The tracer initialization is carried out with customized modules in Si3D, which are based on the turbidity profiles at multiple locations obtained from the field measurements. The purpose of adding tracers in the model is to facilitate an intuitive comparison with the constituent data (i.e., turbidity) measured in the field and to visualize the 3-D effects of artificial mixing in the model. The tracer initialization calculates the initial profiles for the 3-D domain in Si3D according to the distributed data obtained from in situ measurements, which adopts the nearest-neighbor interpolation method that is common in scattered data approximation to fill in data gaps (Parker et al., 1983). Subsequently, the module in Si3D assigns the initial 3-D profiles across the entire computational domain immediately after the model has been allowed to spin up and before a numerical experiment commences.

2.2.3. Coupled Model Validation

The Si3D hydrodynamic model, coupled with the water-jet and bubble-plume models is validated with the field data. The comparison focuses on the physical processes (i.e., variation of thermal structure) associated

with the operation of both the SSS and EM systems. Details of the comparison and validation can be found in supporting information section S2.

Overall, the results show that the numerical model is able to make good prediction of the vertical thermal structure when the two systems are in concurrent operation. The difference between the field and numerical data in the mean temperature for the entire water column during EM1 was only ~1.8% of the mean field temperature during the simulated period, with a root-mean-square-error (RMSE, refer to the calculation in supporting information section S1) of the temperature variation between the field and simulation data of ~0.9 °C.

2.3. Comparative Indicators

Various lake-specific indices, which are calculated according to the procedures reported in the literature, are adopted in the subsequent discussion. These parameters include mixed layer depth (the lower metalimnetic boundary), Schmidt stability, and weighted average values for environmental constituents (i.e., turbidity level) throughout the water body. Details of the calculation procedures are provided in supporting information section S1 (Idso, 1973; Imberger, 1985; Fee et al., 1996; Read et al., 2011).

3. Results and Discussion

The present investigation aims to identify changes in the thermal structure, DO, and potential transport mechanisms under various operational conditions at a whole-reservoir scale. The 3-D spatial profiles of temperature and DO across both the longitudinal section and lateral transects (i.e., Transects #1–#4) are examined as a function of the EM flow rate. The longitudinal section provides an overview of 3-D mixing across the reservoir from the shallow (FCR10) to the deep (FCR50) region, whereas the transects elucidate lateral effects of the mixing near the diffuser. The development of the thermal structure at the individual water columns (FCR10-FCR50) over time is also discussed. Finally, the constituent transport across the reservoir is investigated.

3.1. Spatial Effects of Mixing

The results obtained during EM1 reveal that the extent to which the thermal structure across the reservoir varies under the influence of artificial mixing is dependent on the distance from the mixing system (Figure 2). Results from EM2 and EM3 show a similar trend and are not presented here. The impact of the different flow rates from EM1-EM3 will be discussed in the following subsection. Figures 2a and 2b of the longitudinal section show that the water temperature tended to be homogenized by epilimnetic mixing in the metalimnion above the EM diffuser, which was consistently predicted by the numerical model (refer to supporting information Figure S2 for the numerical contours). The thermal structure in the field responded quickly to the epilimnetic mixing. The lower metalimnetic boundary across the deep region was noticeably deepened by the epilimnetic mixing as shown in Figures 2a and 2b (red dashed lines), with a maximum depth variation of over 0.5 m within the first 2 h of mixing. The mixing energy propagated rapidly toward the shallow region of the reservoir although the EM diffuser was deployed in the deep region. In comparison with the profiles before the epilimnetic mixing, variation of the thermal structure in the mixed layer is successively smaller from the deep to shallow regions, suggesting a reduced impact of mixing on the thermal structure beyond the location of the EM diffuser. Although the SSS system was in operation during the investigated period, no obvious effect of the SSS operation on the thermal structure in the hypolimnion was observed in the longitudinal thermal structure.

The temperature profiles across Transect #1 (Figures 2c and 2d), located across the EM diffuser reveal the instantaneous thermal structure variation that occurred within 2 h after epilimnetic mixing began, in the absence of any substantial weather event (e.g., storms). The results in the thermal contours show that the thermal structure above the EM diffuser in the metalimnion was altered by the epilimnetic mixing, with the greatest effects on the thermal structure immediately above the EM diffuser. The contours reveal that the mixing processes involved the cold water near the EM diffuser being carried up toward the surface of the water body by the plume. At the DMPR, the cold water that previously entrained into the plume was detrained to adjacent water horizontally. The field data suggest that the detrainment of the plume-mixed water at the DMPR reduced the temperature gradient in the neighboring water columns compared to the

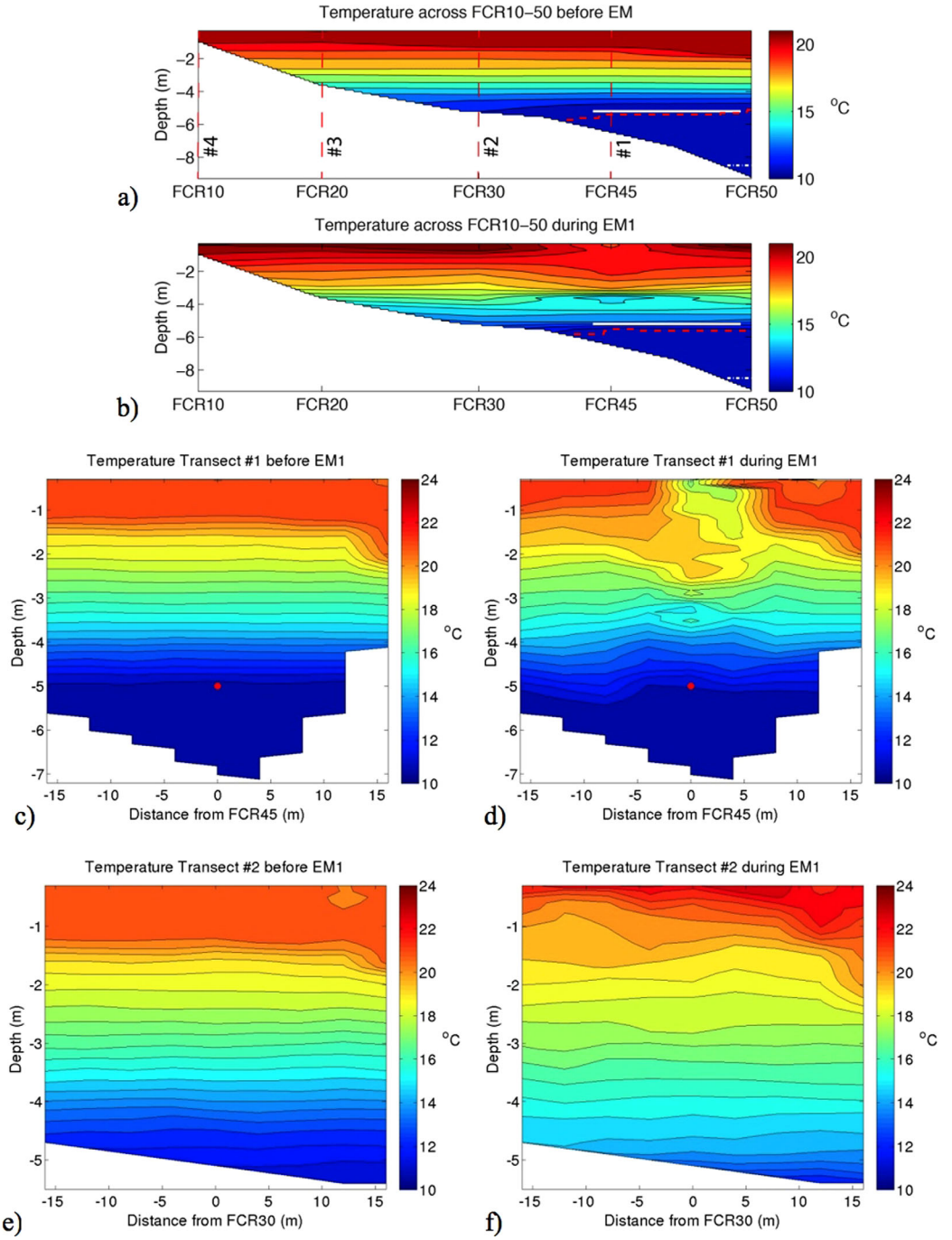

Figure 2. Field thermal structure in FCR measured before and during EM1. Longitudinal section: (a) before EM1 on Day 150; (b) during EM1 with 2 h operation. Please note that #1–#4 in Figure 2a indicate the relative locations of Transects #1–#4 along the section. White solid and dashed lines indicate the relative locations of the EM and SSS diffusers, respectively. Red dashed line indicates the depth of the lower metalimnetic boundary based on the field data. Transect #1: (c) before EM1 and (d) during EM1 with 2 h operation. Transect #2: (e) before EM1 and (f) during EM1 with 2 h operation. The red dot in Figures 2c and 2d indicates the location of the EM diffuser through the transect.

center of the plume. A corresponding pattern of compacted isotherms in the metalimnion above the EM diffuser can be identified in the isotherms shown in Figures 2c and 2d.

The DO profiles from Transect #1 also reveal the aforementioned impact of epilimnetic mixing on water (Figure 3). The contours in Figures 3a and 3b show enhanced exchange of DO near the interface of the

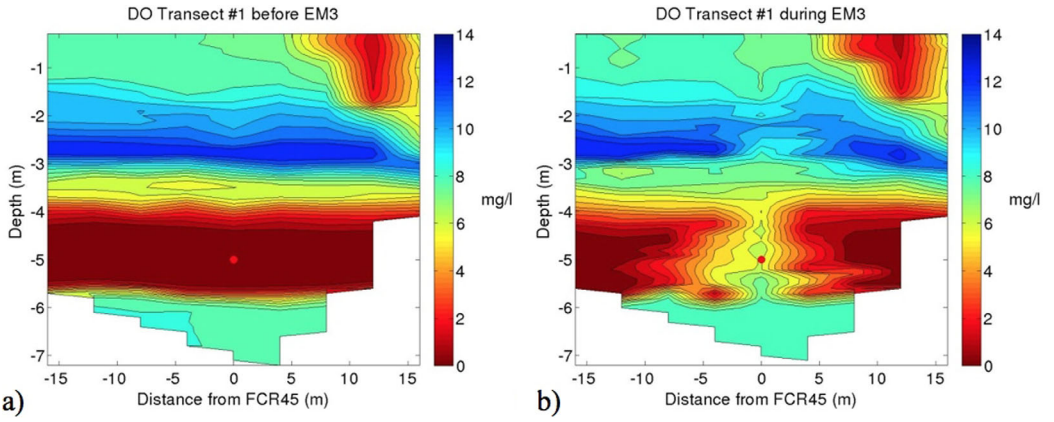

Figure 3. Field DO profiles at Transect #1 (a) before and (b) during the EM system in operation for 2 h in EM3. The red dot indicates the location of the EM diffuser through the transect.

hypolimnion and mixed layer between −6 and −5 m, which tends to homogenize the DO across the region of Transect #1. While the DO above the EM diffuser was effectively increased, the average DO concentration well below the diffuser in the hypolimnion (<−6 m) was hardly affected, as indicated in Figure 3b. Therefore, the epilimnetic mixing has a large impact on DO distribution above the EM diffuser, but has limited impact on the hypolimnetic water.

The thermal structures before and during the EM1 experiment at Transect #2, immediately upstream of the diffuser, further demonstrate that the effects of the epilimnetic mixing became weaker in the shallow water compared to the deep water (i.e., Transect #1), as suggested by the isotherms (Figures 2e and 2f) with weaker water temperature response. Compared with the temperature profiles before the epilimnetic mixing took place, the water temperature near the bottom of Transect #2 increased by about 1°C during the epilimnetic mixing even though the surface water temperature did not change significantly with a mean surface temperature increase of less than 0.1°C. The increased temperature near the bottom was due to the effect of the epilimnetic mixing (see the following subsection). Compared to Transect #1, the overall impact of the epilimnetic mixing on the thermal structure at Transect #2 was much lower. Since Transect #3 and Transect #4 were further away from the diffuser at shallower depths, the response of thermal structure to epilimnetic mixing was minimal, as indicated by Figure 2b. Apart from the epilimnetic mixing, the observed effects of mixing induced by the SSS system were not distinct because all the transects were beyond the SSS distribution header.

3.2. Flow Rate Effects on Mixing

The 3-D thermal structure under the influence of epilimnetic mixing varied for the three different flow rates from EM1–EM3. The two transects (#1 and #2) near the EM diffuser are in focus here.

At Transect #1, shown in Figures 4a–4c, the plume boundaries (defined by the plume width and DMPR) during epilimnetic mixing in each case with the different flow rates are depicted by the blue curved lines. Both the plume width and DMPR were calculated in the bubble-plume model and obtained as output parameters from Si3D. Figures 4a–4c shows that the plume boundary estimated by the model is closely associated with the patterns of compacted isotherms induced by the epilimnetic mixing, as expected. The observation from the three sets of contours in Figures 4a–4c confirms that the maximum depth of the water column affected by the epilimnetic mixing decreased, with the flow rate of the EM system reduced in each experiment while thermal stability steadily increased in summer. The pattern of compacted temperature isotherms in the metalimnion generally agrees with the plume boundary predicted by the model. Based on the pattern shown in the temperature contours from the field measurements, the DMPRs for the three different EM flow rates were estimated by finding the water depth below the epilimnion (<−1 m), where the difference between the in-plume temperature (at 0 m from the diffuser) and the average temperature of the two horizontally neighboring measurement points (at ±4 m from the diffuser) is the greatest. The estimated field DMPRs at the beginning of mixing were at ∼−2.1 m for 708 LPM or 25 standard cubic feet per minute (scfm), ∼−3.2 m for 425 LPM (15 scfm), and ∼−3.9 m for 198 LPM (7 scfm), respectively. The field

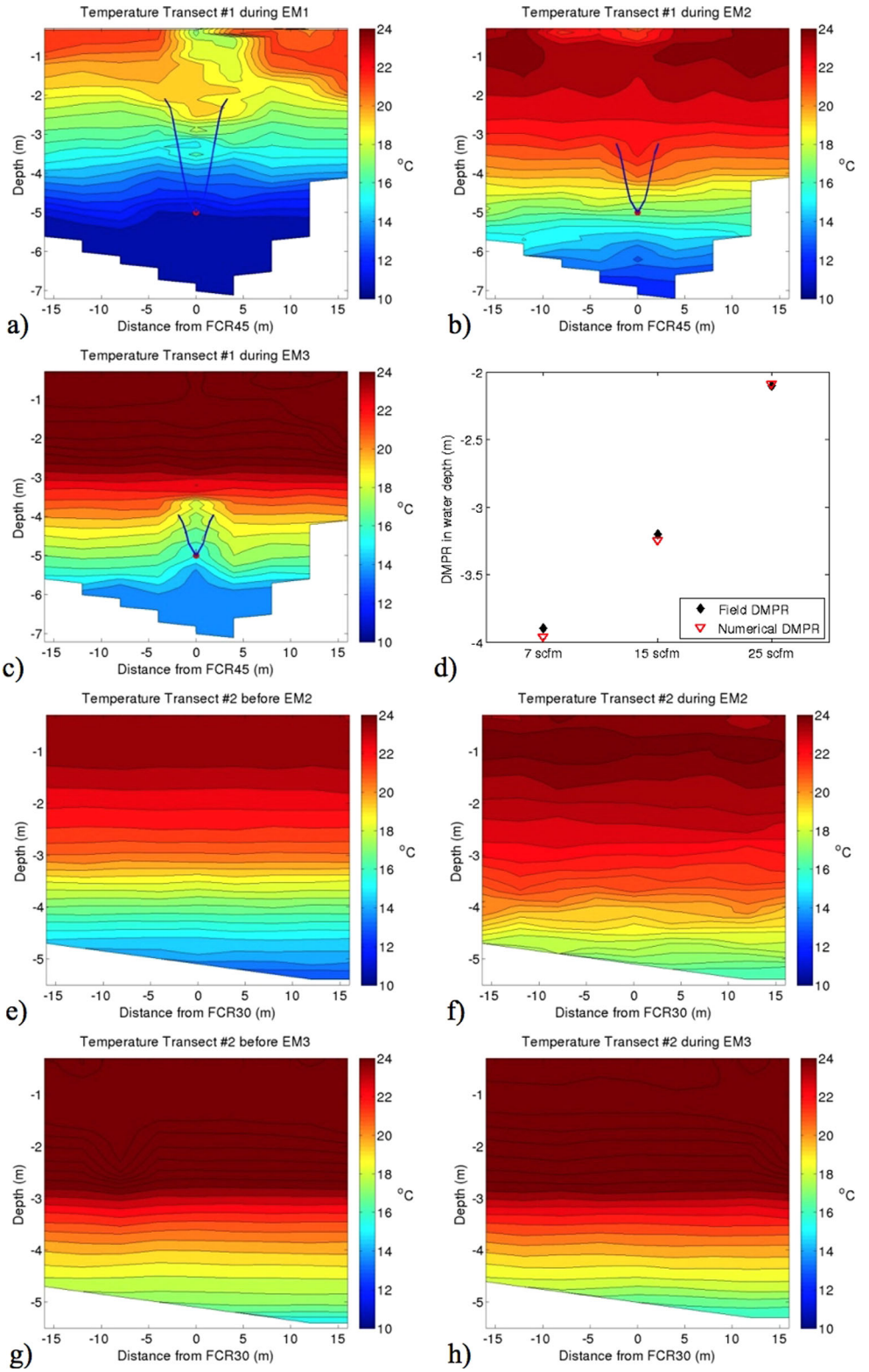

Figure 4. Field thermal structures and DMPRs from the transects of FCR. Transect #1 during: (a) EM1, (b) EM2, and (c) EM3 with 2 h operation; pair of blue curved lines in each contour represents the model-estimated structure of the plume during the operation of the EM system. (d) Field DMPR estimated from the temperature profiles versus numerical DMPR obtained from the bubble-plume model in Si3D. Transect #2: (e) before EM2 and (f) during EM2 with 2 h operation; (g) before EM3 and (h) during EM3 with 2 h operation.

results are consistent with the predicted DMPRs as shown in Figure 3d, which has an adjusted R-squared of 0.99 and RMSE of 0.013 m. The results demonstrate that the region with heterogeneous thermal structure above the EM diffuser during epilimnetic mixing is closely associated with the characteristics of the plume structure. Since the plume structure depends on the EM flow rate, the EM flow rate is an important factor to control the extent of mixing at Transect #1.

Consistent with what was mentioned in section 3.1, the water temperature near the bottom of Transect #2 increased during epilimnetic mixing, which can be seen in all three EM experiments (Figures 2e, 2f, and 4e–4h). The results confirm that the temperature increase near the bottom of Transect #2 was caused by the epilimnetic mixing and was associated with the mixing intensity, i.e., the EM flow rate. The impact of the mixing in the deep region may propagate toward the shallow region (i.e., Transect #2), which tends to mix the water near the bottom of the shallow region. In addition, it is evident at Transect #2 beyond the EM diffuser that the extent of mixing also depends on the EM flow rate, and it reduces with the decreasing EM flow rate.

3.3. Time Series of Mixing

Figure 5 shows that the epilimnetic mixing consistently deepened the lower metalimnetic boundary in most of the regions in the reservoir during all three EM experiments, resulting in a reduced Schmidt stability at a rate of $-17\ \mathrm{J/(d \cdot m^2)}$ during EM1. The impacts of the epilimnetic mixing on the temperature gradient in the metalimnion were successively decreased while moving from the deep region (FCR50 and FCR45) to the shallow region (FCR20). Although the mixing intensity of EM2 was smaller than EM1, the lower metalimnetic boundary was deepened more substantially in EM2 than in EM1 at the beginning of the epilimnetic mixing. This was due to the combined effects of the mixing induced by the EM system and an unexpected storm which occurred during the early stage of EM2 (refer to supporting information Figure S1).

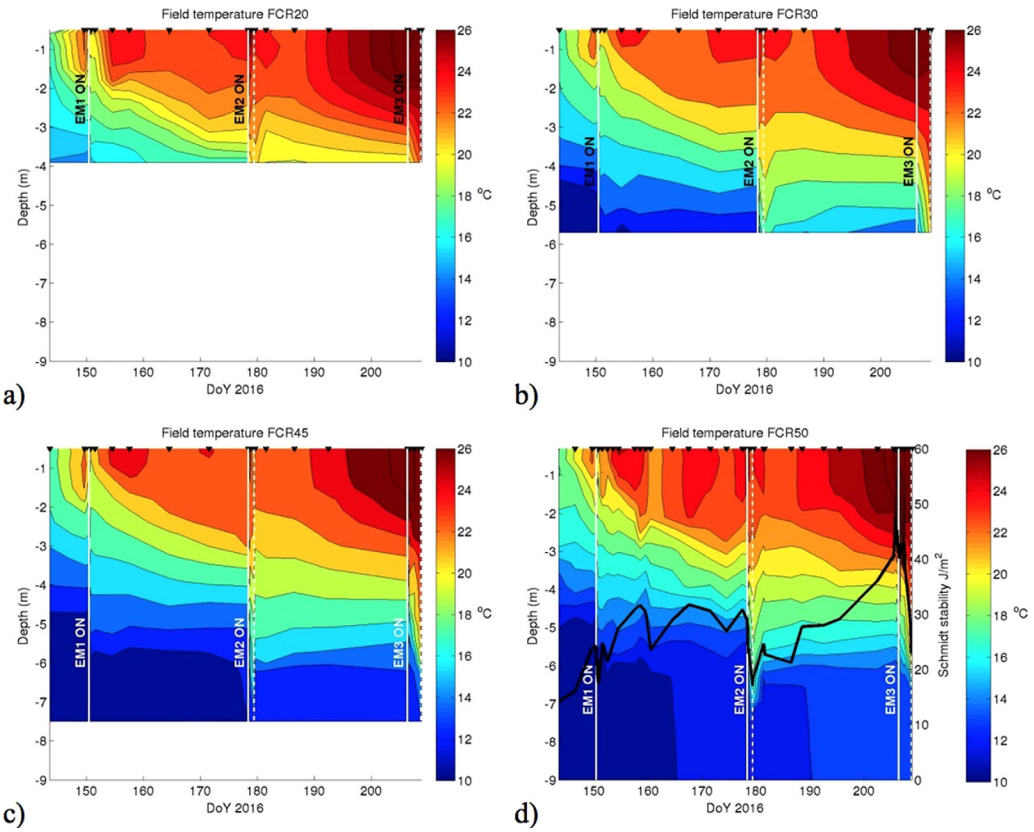

Figure 5. Time series of field water temperature profiles for (a) FCR20, (b) FCR30, and (c) FCR45; (d) FCR50 with Schmidt stability shown as the black line. All contours are plotted on the same depth, time, and temperature scales.

The continuous operation of the SSS system in the hypolimnion throughout the field experiments did not destratify the water body, as shown in Figure 5d. The hypolimnetic temperature at FCR50 was vertically uniform and increased slightly during the summer, which is consistent with the previous study (Gerling et al., 2014). The hypolimnetic temperature at FCR45 (Figure 5c) increased at a slower rate than that at FCR50, as suggested by the vertical isotherms in the hypolimnion, indicating that the influence of the mixing induced by the SSS system was weak and limited to the region close to the distribution header in the hypolimnion. The sites beyond the SSS distribution header (FCR10–20) were not affected by the SSS system because the hypolimnion did not extend to these upstream shallow sites. Compared to the epilimnetic mixing that consistently reduced the thermal stability (see Figure 5d), the SSS system in continuous operation over the study period had minimal effects on the thermal structure along the water column, as indicated by the Schmidt stability that generally increased outside the epilimnetic mixing periods at a rate of about 0.87 $J/(d \cdot m^2)$. Comparisons of the field data with the numerical results are shown in supporting information section S2.

Since the SSS system was designed for oxygenating the hypolimnetic water, it is not surprising to see that the system maintained DO concentration in the hypolimnion, as shown in Figures 6c and 6d. The DO concentration decreased after Day 160 when the oxygen delivery rate was reduced by approximately one half due to the high DO saturation level in the hypolimnion (refer to Figures 6c and 6d). Even with the reduction of the oxygen delivery rate, the DO level in the hypolimnion remained high (over 8 mg/L). However, a metalimnetic minimum DO (MMDO) (Kreling et al., 2017; Morris et al., 1982; Shapiro, 1960) developed in the lower metalimnion during the operation of the SSS system, as seen in Figures 6c and 6d. This was caused by the weak vertical mixing induced by the SSS system with its jet nozzles pointing almost horizontally, which has limited capacity to transport DO vertically toward the metalimnion (Gerling et al., 2014). Although the SSS system eliminated hypoxia in the hypolimnion, sediment oxygen uptake continuously consumed the DO in the bottom water of the shallow region and laterally across the layer at around −5 m depth

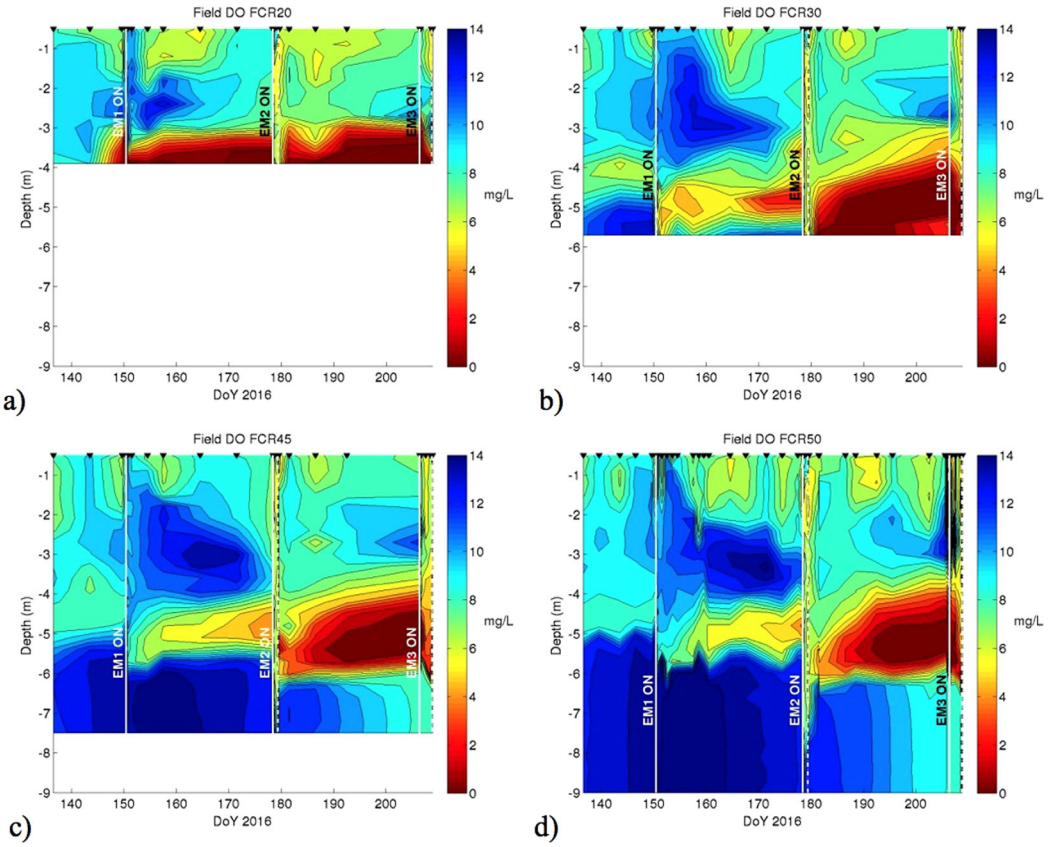

Figure 6. Time series of field DO profiles for (a) FCR20, (b) FCR30, (c) FCR45, and (d) FCR50. All contours are plotted on the same depth, time, and DO concentration scales.

during the summer. As a consequence, later in the summer, a more severe MMDO was formed in the deep region with the lowest DO concentration at zero because of DO depletion by the process mentioned above.

Conversely, the epilimnetic mixing by the EM system tends to disrupt the development of the MMDO. In Figure 6, distinct mixing outcomes can be observed where the magnitude of the MMDO was temporarily alleviated during each operation of the EM system. Based on the observation in Figure 6, the three periods of epilimnetic mixing did not substantially increase the overall DO concentration. However, it shows that the epilimnetic mixing enhanced oxygen transfer near the lower boundary of the metalimnion, the result of which can be seen in Figure 3. Consistent with the observation in the thermal contours in Figure 5, the influence of mixing on the DO level is reducing toward the shallow region. It is believed that the combined operation of the two systems in an appropriate manner could be used to improve the DO level in the lacustrine region where the diffusers are deployed without causing premature destratification.

To further analyze the 3-D influence of epilimnetic mixing, the depth of the lower metalimnetic boundary (refer to supporting information section S1) was estimated (Figure 7). The figure reveals that the thermal structures from FCR30–FCR50 were strongly affected by the operation of the EM system. It is not surprising to see that FCR45 and FCR50 experienced the same level of mixing, with the deepening rates of the lower metalimnetic boundary at −0.12 m/h during EM1, −0.06 m/h during EM2, and −0.02 m/h during EM3 (the negative values indicate that the boundary moves toward the water bottom), as shown in Figures 7b and 7c. The effect of the epilimnetic mixing was more distinct in the deep region where the diffuser is deployed (i.e., FCR45). For comparison, the deepening rate of the lower metalimnetic boundary at FCR30, which is about ∼120 m away from the diffuser, was approximately 55% lower on average for the three experiments. The response of the lower metalimnetic boundary was rapid and substantial during the epilimnetic mixing, which can be seen in the enlarged plot during EM1 shown in Figure 7c. A similar trend was also reported in (Chen et al., 2017). However, due to the storm mentioned above (Figure 5), the lower metalimnetic

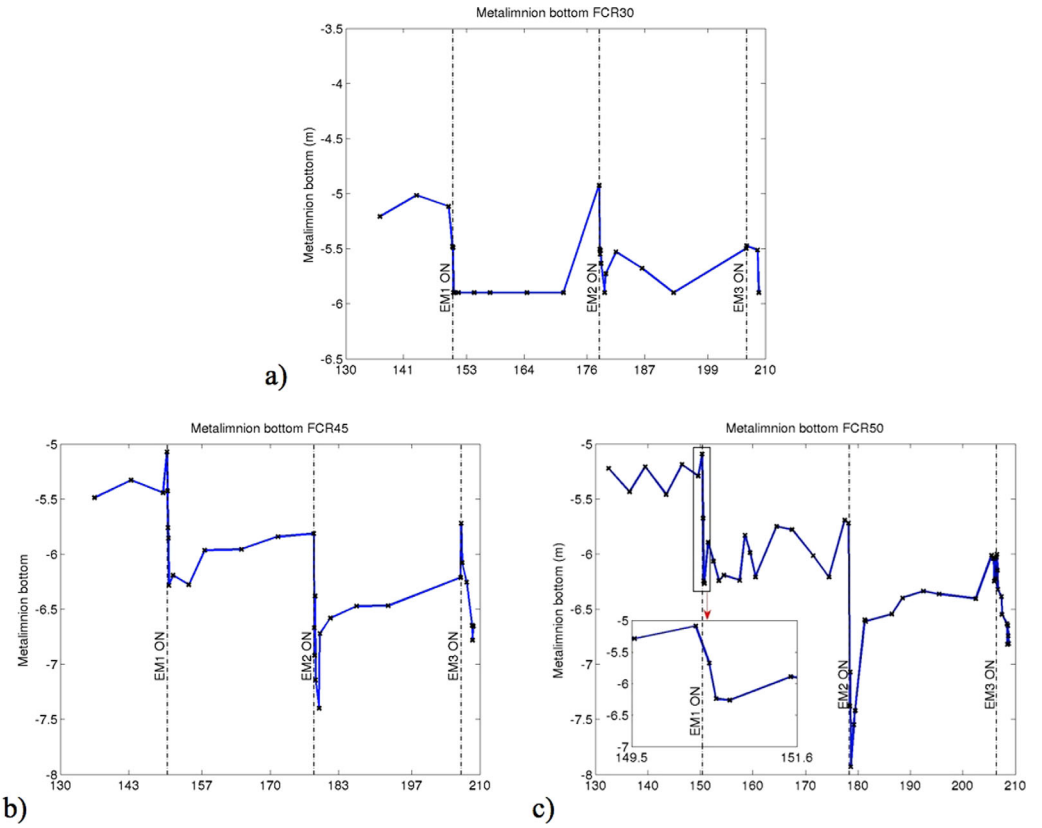

Figure 7. Time series of the depth of the lower metalimnetic boundary based on the field thermal structure for (a) FCR30, (b) FCR45, and (c) FCR50, respectively. The inset of enlarged plot shows the EM1 period at FCR50. Note the difference in y axes between Figure 7a and Figures 7b and 7c.

boundary in the deep region (FCR45 and FCR50) during EM2 was deepened by ~2 m, even though the mixing flow rate and the operation duration were lower and shorter than the other EM experiments (Tables 1 and 2). The sharp deepening of the boundary may be due to a strong seiche caused by the storm.

Overall, the results show that, while the SSS system works according to its design goals with no distinct 3-D effects on the thermal structure and with DO added to the hypolimnion only, the EM system at the tested flow rates has substantial 3-D impacts across the horizontal extent of the reservoir, altering the thermal structure and redistributing the DO. The epilimnetic mixing induced by the EM system will therefore be the focus in the subsequent analysis of constituent transport.

3.4. Constituent Transport

In the subsequent analysis, field data and numerical results are first compared and discussed to reveal the transport mechanism for constituents in the water body under the influence of epilimnetic mixing. A numerical case study is then carried out to determine constituent transport with longer-term epilimnetic mixing imposed under different mixing intensities. The numerical case study focuses on factors that control constituent transport across the water body.

3.4.1. Experimental Data Analysis

Constituent transport processes may reflect the movement of pollutants as a result of the flows induced by the EM system. A common indicator for this purpose is turbidity, which is a measure of the quantity of particles suspended in water that scatter light and reduce transparency (Lewis, 1996; Holliday et al., 2003). It is found that the total constituent concentration in water was conserved during the relatively short epilimnetic mixing periods, as suggested by the estimated total turbidity levels during the three EM experiments (refer to supporting information section S3, Taylor, 1997, and Figure S7). Therefore, the field turbidity data are used in the subsequent analysis to visualize the constituent transport induced by epilimentic mixing and then compared to the results obtained from numerical tracers using the validated Si3D coupled hydrodynamic model.

The field turbidity contours reveal that the flow induced by the EM system carried the high-turbidity water from the shallow region to the deep region in the metalimnion (Figure 8). In Figure 8c, the turbidity in the water layer between the depth of the EM diffuser line (−5 m) and the DMPR (−2 m) was dispersed by the flow induced by the epilimnetic mixing. The high-turbidity water in turn traveled along the sloping bottom from the shallow region toward the deep region near the depth of the EM diffuser during the epilimnetic mixing.

In the simulation, passive tracers were added in the Si3D model to verify the field observation of turbidity movement. The tracer was initialized three dimensionally as described in section 2.2, based on the distribution of the field turbidity data before EM1. The numerical tracer distribution before the epilimnetic mixing resembled the field turbidity distribution before mixing (Figure 8a). Due to the complexity of the turbidity distribution in the field and the relatively limited measurement data available across the reservoir, the numerical contours of turbidity before the epilimnetic mixing varied somewhat from the field turbidity contours. Nevertheless, the field and numerical contours show consistent overall distribution of turbidity in the reservoir, with a majority of the high-turbidity levels located in the littoral region (Figures 8a and 8b). During the EM mixing period, consistent transport of turbidity can be observed in both the field and numerical data, suggesting a counter-clockwise circulation between FCR20 and FCR45 that was induced by the operation of the EM system in the metalimnion (Figures 8b and 8d). It is thus concluded that the induced circulation by the EM mixing enhances constituent exchange in the metalimnion between the shallow and deep regions, as suggested in Figures 8a–8d.

The predicted vertical distribution of tracer at FCR30 is compared to the turbidity results from EM1 at the selected time instants in Figure 8e. If FCR30 is considered as an approximate boundary that separates FCR into shallow and deep regions, the variation of the vertical profiles in FCR30 may indicate how the constituents are exchanged between the two regions under the effect of the epilimnetic mixing. A similar trend before and during the epilimnetic mixing can be obtained from the vertical distribution of both the field turbidity and numerical tracer data, as shown in Figure 8e. The result confirms the observation in the field and the numerical contours in Figures 8a–8d, which shows that constituents were transported by a counter-clockwise circulation induced by the epilimnetic mixing through the lower metalimnion from the shallow region to the deep region.

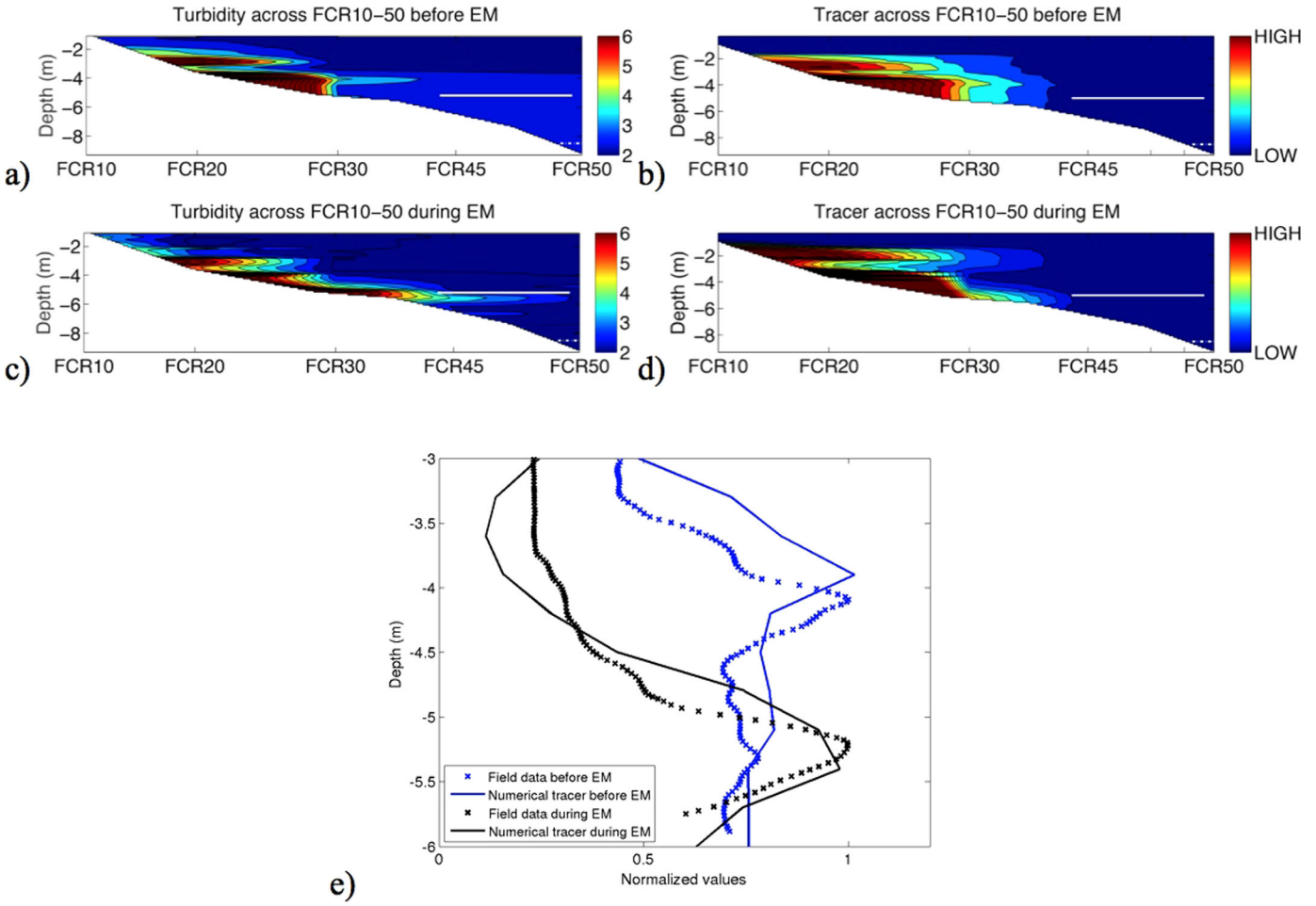

Figure 8. The longitudinal section in FCR: (a, c) Field turbidity before and during (2 h) epilimnetic mixing (in NTU), and (b, d) numerical tracer before and during epilimnetic mixing; white solid and dashed lines indicate the relative locations of the EM and SSS diffusers, respectively. (e) Field turbidity versus numerical tracer at FCR30 before and during (2 h) EM1 in normalized values with regard to the maximum values of the time instant.

Therefore, the present investigation identifies the enhancement of constituent transport across the reservoir under the effect of epilimnetic mixing, which facilitates the transport of constituents horizontally from the littoral region (often brought in by runoff) into the deep region of the reservoir. The results also show that the coupled Si3D model made a reasonably good prediction of the constituent transport induced by the epilimnetic mixing.

3.4.2. Numerical Case Study

Based on the aforementioned comparisons between the field data and the model-predicted results, the coupled Si3D hydrodynamic model is considered appropriate for estimating three-dimensional tracer movement when mixing is imposed on the water body. Since the mixing induced by the SSS system did not have a substantial effect on the flow and thermal structure over the majority of the water body, the present numerical case study employs Si3D to visualize the tracer dispersing processes with only the EM system in operation for an extended period.

In this investigation, tracers are added to the computational domain with the flows induced by the bubble plume over the entire period of artificial mixing. The flow rate of the tracers is adjusted depending on the flow rate from the EM diffuser in the model to visualize the region under the influence of epilimnetic mixing in the computational domain. The variation of the tracer concentration in each grid cell is handled by the hydrodynamic model as a passive scalar after injection. The total period of the numerical simulation is 4 days, with the EM system in continuous operation from Day 2 to Day 4 in simulation. The meteorological input uses a set of repeated data from a calm day (Day 160) in the mid-summer to avoid mixing induced by

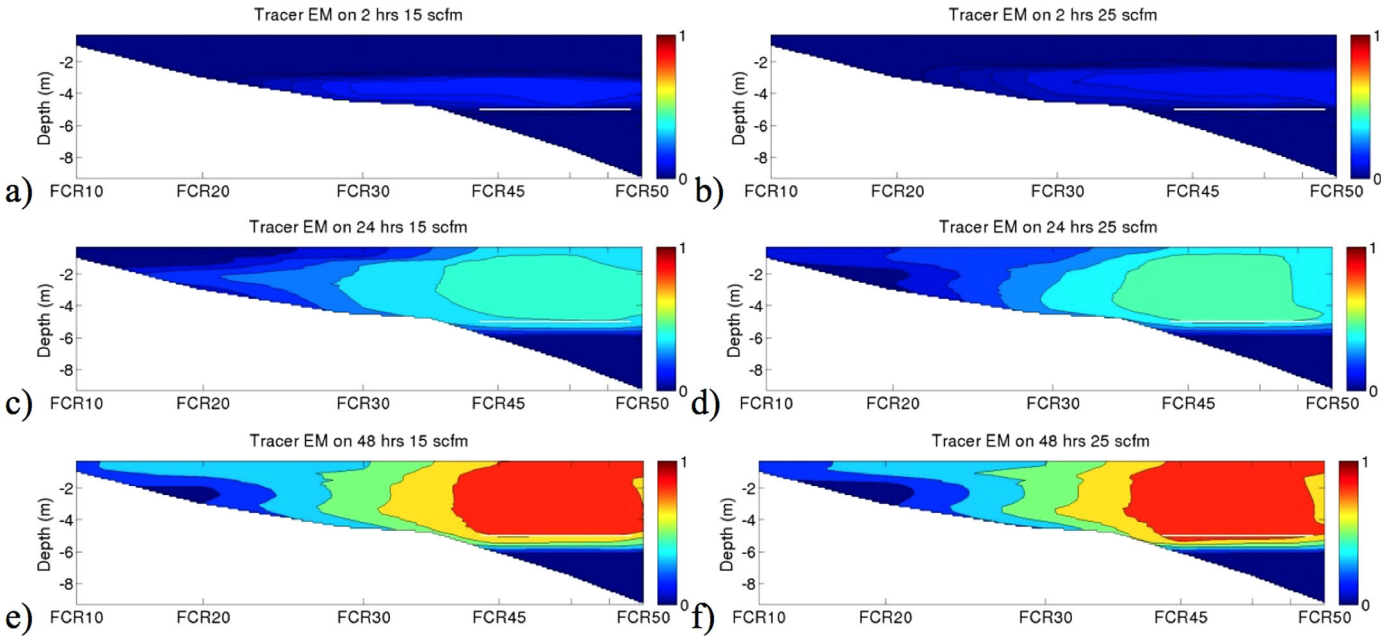

Figure 9. Instantaneous response of numerical tracer concentration in FCR: (left) EM flow rate at 425 LPM (15 scfm); (right) EM flow rate at 708 LPM (25 scfm). The tracer concentration is normalized by the maximum concentration during the experimental period.

storms. Two EM flow rates are tested with a low flow rate at 425 LPM (15 scfm) and a high flow rate at 708 LPM (25 scfm).

The time series of the tracer distribution in terms of the longitudinal profiles is shown in Figure 9 for both cases with the different flow rates. The instantaneous distribution of the tracer after the EM operation begins (Figures 9a and 9b) suggests that, with the higher flow rate, the longitudinal extent of the region affected by the EM operation is greater than that with the lower flow rate. This is mainly due to the variation of the DMPRs at the different flow rates. After 1 day operation of the EM, most of the area in the deep region of FCR is affected by the epilimnetic mixing at both flow rates (Figures 9c and 9d). However, the surface layer in the shallow region (i.e., FCR10 and FCR20) is hardly affected in the case with the lower flow rate, where the impact by the epilimnetic mixing is 64% lower in terms of the average tracer concentration between FCR10 and FCR20. This is due to the relatively lower DMPR and less energy dissipation associated with the epilimnetic mixing at the lower flow rate. Subsequently, after 2 days of continuous epilimnetic mixing (Figures 9e and 9f), tracers have reached most of the water body across the longitudinal section. Interestingly, the distribution of tracer concentration is almost the same for both flow rates. The results suggest the importance of the duration of EM operation, and reduced importance of the EM flow rate. Specifically, if the interest is in long-term epilimnetic mixing, the effect of the flow rate on constituent transport along the longitudinal section is not as important as the duration of operation to consider.

The tracer distribution along Transect #1 in Figure 10 suggests a similar trend of tracer development as shown in Figure 9. In Figures 10a–10f, the epilimnetic mixing at both flow rates rapidly affects the region close to the depth of the EM diffuser at Transect #1, and the effect is stronger with the higher flow rate. Furthermore, Figures 10a–10f shows that the EM operation has very limited influence on the hypolimnetic water well below the EM diffuser (<-6 m) in terms of constituent transport, even after 2 days of operation. This is consistent with the field DO data shown in Figure 3b, where the DO level in the hypolimnion was mostly unaffected by the epilimnetic mixing. In the shallow region that is far beyond the EM diffuser (Transect #3 shown in Figures 10g and 10h), the delay in response to the mixing can be observed after 2 h operation in both cases. The results show that the tracer reached the bottom of the shallow region more quickly with the higher flow rate because of the stronger energy dissipation induced by the artificial mixing.

The present numerical case study of tracer transport confirms that the artificial mixing processes occurred three dimensionally in the water body, with a delay in response to the mixing in the shallow region beyond

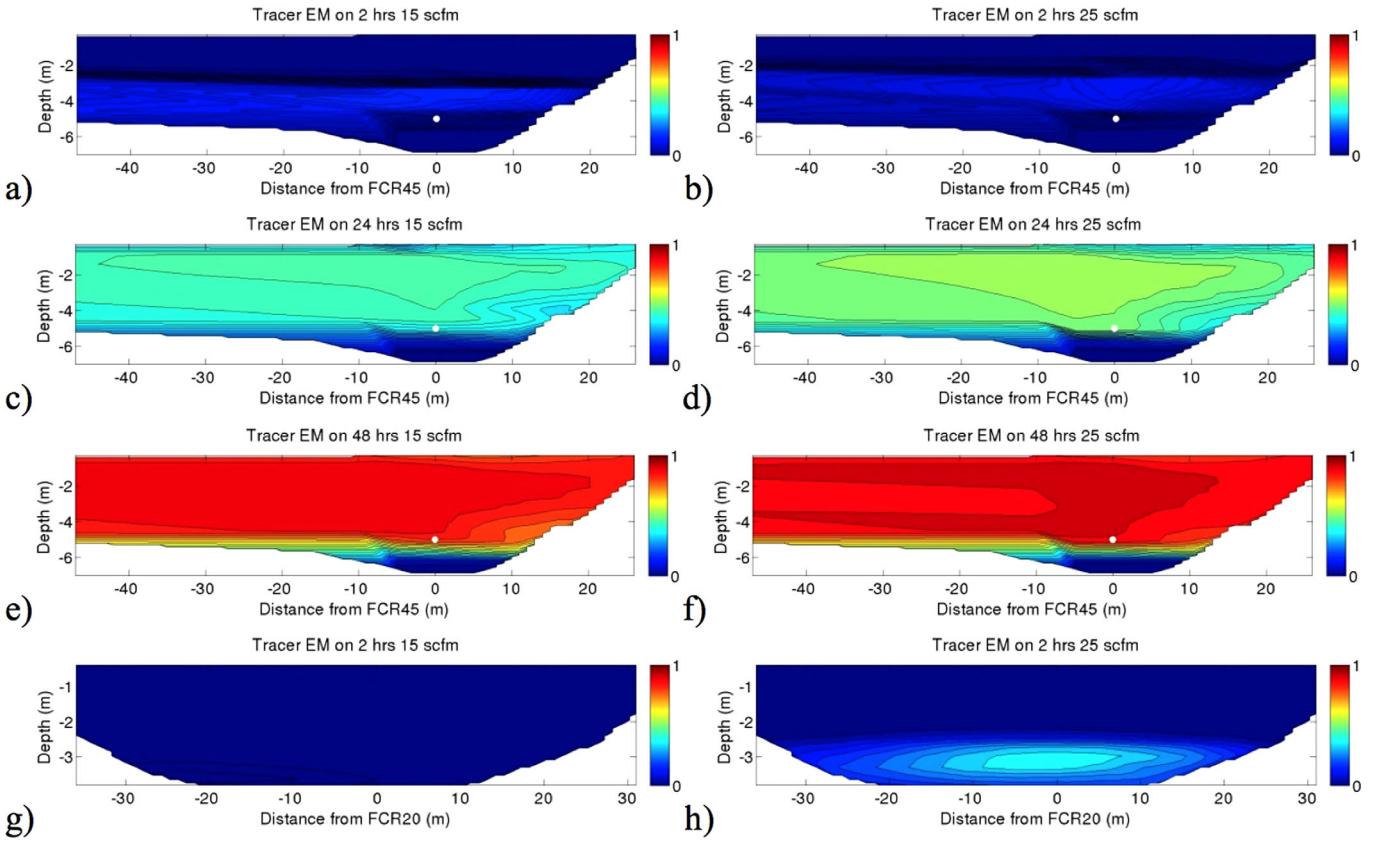

Figure 10. Instantaneous response of numerical tracer along (a–f) Transect #1 and (g, h) Transect #3. (left) EM flow rate at 425 LPM (15 scfm); (right) EM flow rate at 708 LPM (25 scfm). The white dot in the contours indicates the relative location of the EM diffuser line. The tracer concentration is normalized by the maximum concentration during the experimental period.

the diffuser. In addition, both the operational flow rate of the EM system and the duration of its operation can affect constituent transport in the water body. While the EM flow rate is a dominant factor for constituent transport over a relatively short period of operation ($\sim$1 day), the duration of EM operation becomes more important to the mixing outcome than the EM flow rate under continuous epilimnetic mixing over an extended period ($>$2 days). The numerical study has demonstrated the necessity of using 3-D numerical models to investigate the constituent transport induced by artificial mixing because 1-D and 2-D models are unable to account for the heterogeneity in water bodies caused by artificial mixing.

4. Conclusions and Recommendations

The present study investigated two water-quality management devices in a relatively small and shallow drinking-water reservoir by adopting a three-dimensional approach for both the field experiments and numerical modeling. The outcomes from the artificial mixing are investigated at the whole-reservoir scale. While the mixing induced by the SSS system does not have a substantial effect on the overall thermal structure, the epilimnetic mixing by the EM system causes heterogeneity in thermal structure, DO concentration, and constituent transport in the reservoir. The epilimnetic mixing not only affects the longitudinal thermal structure, but also enhances the transport of constituents between the shallow and deep regions. The thermal structure and DO concentration across the transect immediately above the EM diffuser are substantially affected during the EM experiments. The temperature gradient and DO distribution in the metalimnetic water are homogenized by the mixing, with the strength of the influence depending on the EM flow rate. In addition, the epilimnetic mixing deepens the lower metalimnetic boundary (with the deepening rate decreased by 55% at a location 120 m upstream from the EM diffuser) and reduces the Schmidt stability near the EM diffuser at a rate of -17 J/(d $\cdot$ m^2) at the highest flow rate. The mixing may alleviate the MMDO that builds up during the summer by enhancing vertical constituent exchange in mixed layers.

Due to the high cost of field experiments and the uncertainty in field experiments caused by weather, 3-D numerical models are useful tools for analyzing artificial mixing in order to improve the design and operation of the mixing systems. Complex weather conditions in the field may have substantial influence on the thermal structure (refer to supporting information section S2), which makes it harder to examine the outcome of artificial mixing with field data alone. A calibrated numerical model is therefore necessary when investigating artificial mixing. In the present study, comparison of the numerical results with the field data suggests that the coupled Si3D hydrodynamic model provided consistent predictions of the 3-D thermal structure and transport of constituents during artificial mixing. Furthermore, the numerical case study of tracers using Si3D has revealed that the operational flow rate of the EM system is an important driver of constituent transport over short-term operation (∼1 day), whereas the duration of the operation becomes dominant if the operation lasts longer than 2 days. In addition, the epilimnetic mixing has limited influence on constituents in the hypolimnion regardless of the operational flow rate and duration.

The present 3-D experimental and numerical investigations of artificial mixing provide insights for understanding the outcomes from the mixing devices in operation. The enhancement of constituent exchange induced by epilimnetic mixing can be beneficial to evenly spread DO across the metalimnion of the water body, thereby reducing the MMDO and hypoxia. It may also help to flush algal species from the shallow regions of the water body, which usually have sufficient light (photic zone) and nutrients (Holmes, 1957), to the deeper regions, where the availability of light and nutrients is often limited (aphotic zone). However, it is clear from the present investigations that improper mixing may introduce constituents (i.e., nutrients or pollutants), which could be trapped in littoral regions, into the bulk water, which may impair water quality. Reservoir managers need to consider the interaction between the deep and shallow regions associated with mixing in lakes and reservoirs when operating artificial mixing systems. Finally, the study reveals that even in a relatively small water body such as FCR, artificial mixing is inherently 3-D in nature, which must be taken into account when artificial mixing in reservoirs is investigated.

Acknowledgments

We thank J. Doubek, C. Harrell, M. Ryan, and S. Kapletzki for their assistance with field data collection. We thank the staff at the Western Virginia Water Authority for support of this research, especially R. Benninger, J. Booth, C. Brewer, P. Martin, J. Morris, and G. Robertson. We also thank the Reservoir Group at Virginia Tech for their thoughtful comments regarding the project. P. Gantzer and M. Mobley provided critical help in the field with the SSS and EM systems. We acknowledge financial assistance from the School of Civil Engineering, The University of Sydney, and the Department of Civil and Environmental Engineering, Virginia Tech. This research was also supported by the Fralin Life Sciences Institute and Global Change Center at Virginia Tech.

References

Becker, A., Herschel, A., & Wilhelm, C. (2006). Biological effects of incomplete destratification of hypertrophic freshwater reservoir. *Hydrobiologia*, *559*(1), 85–100.

Chen, S., Lei, C., Carey, C. C., Gantzer, P. A., & Little, J. C. (2017). A coupled three-dimensional hydrodynamic model for predicting hypolimnetic oxygenation and epilimnetic mixing in a shallow eutrophic reservoir. *Water Resources Research*, *53*, 470–484. https://doi.org/10.1002/2016WR019279

Cole, T. M., & Wells, S. A. (2006). *CE-QUAL-W2: A two-dimensional, laterally averaged, hydrodynamic and water quality model*, Version 3.5. Washington, DC: U.S. Army Corps of Engineers.

Davison, W. (1993). Iron and manganese in lakes. *Earth-Science Reviews*, *34*(2), 119–163.

Fee, E. J., Hecky, R. E., Kasian, S. E. M., & Cruikshank, D. R. (1996). Effects of lake size, water clarity, and climatic variability on mixing depths in Canadian Shield lakes. *Limnology and Oceanography*, *41*(5), 912–920.

Fernandez, R. L., Bonansea, M., Cosavella, A., Monarde, F., Ferreyra, M., & Bresciano, J. (2012). Effects of bubbling operations on a thermally stratified reservoir: Implications for water quality amelioration. *Water Science and Technology*, *66*(12), 2722–2730.

Gantzer, P. A., Bryant, L. D., & Little, J. C. (2009). Effect of hypolimnetic oxygenation on oxygen depletion rates in two water-supply reservoirs. *Water Research*, *43*(6), 1700–1710.

Gerling, A. B., Browne, R. G., Gantzer, P. A., Mobley, M. H., Little, J. C., & Carey, C. C. (2014). First report of the successful operation of a side stream supersaturation hypolimnetic oxygenation system in a eutrophic, shallow reservoir. *Water Research*, *67*, 129–143.

Gerling, A. B., Munger, Z. W., Doubek, J. P., Hamre, K. D., Gantzer, P. A., Little, J. C., & Carey, C. C. (2016). Whole-catchment manipulations of internal and external loading reveal the sensitivity of a century-old reservoir to hypoxia. *Ecosystems*, *19*, 555–571.

Harris, L. A., Hodgkins, C. L. S., Day, M. C., Austin, D., Testa, J. M., Boynton, W., . . . Chen, N. W. (2015). Optimizing recovery of eutrophic estuaries: Impact of destratification and re-aeration on nutrient and dissolved oxygen dynamics. *Ecological Engineering*, *75*, 470–483.

Heo, W.-M., & Kim, B. (2004). The effect of artificial destratification on phytoplankton in a reservoir. *Hydrobiologia*, *524*(1), 229–239.

Hipsey, M. R., Bruce, L. C., & Hamilton, D. P. (2013). *GLM—General lake model: Model overview and user information* (AED Rep. 26, 42 pp.). Perth, Australia: University of Western Australia.

Holliday, C., Rasmussen, T. C., & Miller, W. P. (2003). *Establishing the relationship between turbidity and total suspended sediment concentration*. Atlanta: Georgia Institute of Technology.

Holmes, R. W. (1957). Chapter 6: Solar radiation, submarine daylight, and photosynthesis. In J. W. Hedgpeth (Ed.), *Treatise on marine ecology and paleoecology* (pp. 109–128). Boulder, CO: Geological Society of America.

Idso, S. B. (1973). On the concept of lake stability. *Limnology and Oceanography*, *18*(4), 681–683.

Imberger, J. (1985). The diurnal mixed layer. *Limnology and Oceanography*, *30*(4), 737–770.

Imberger, J., Patterson, J., Hebbert, B., & Loh, I. (1978). Dynamics of reservoir of medium size. *ASCE Journal of the Hydraulics Division*, *104*(5), 725–743.

Imteaz, M. A., & Asaeda, T. (2000). Artificial mixing of lake water by bubble plume and effects of bubbling operations on algal bloom. *Water Research*, *34*(6), 1919–1929.

Imteaz, M. A., Shanableh, A., & Asaeda, T. (2009). Modelling multi-species algal bloom in a lake and inter-algal competitions. *Water Science and Technology*, *60*(10), 2599–2611.

Kreling, J., Bravidor, J., Engelhardt, C., Hupfer, M., Koschorreck, M., & Lorke, A. (2017). The importance of physical transport and oxygen consumption for the development of a metalimnetic oxygen minimum in a lake. *Limnology and Oceanography*, *62*(1), 348–363.

Lake, B. A., Coolidge, K. M., Norton, S. A., & Amirbahman, A. (2007). Factors contributing to the internal loading of phosphorus from anoxic sediments in six Maine, USA, lakes. *Science of the Total Environment*, *373*(2), 534–541.

Lewis, J. (1996). Turbidity-controlled suspended sediment sampling for runoff-event load estimation. *Water Resources Research*, *32*(7), 2299–2310.

Morris, A., Loring, D., Bale, A., Howland, R., Mantoura, R., & Woodward, E. (1982). Particle dynamics, particulate carbon and the oxygen minimum in an estuary. *Oceanologica Acta*, *5*(3), 349–353.

Munger, Z. W., Carey, C. C., Gerling, A. B., Hamre, K. D., Doubek, J. P., Klepatzki, S. D., . . . Schreiber, M. E. (2016). Effectiveness of hypolimnetic oxygenation for preventing accumulation of Fe and Mn in a drinking water reservoir. *Water Research*, *106*, 1–14.

Nürnberg, G. K., LaZerte, B. D., & Olding, D. D. (2003). An artificially induced *Planktothrix rubescens* surface bloom in a small Kettle Lake in Southern Ontario compared to blooms world-wide. *Lake and Reservoir Management*, *19*(4), 307–322.

Nürnberg, G. K., Shaw, M., Dillon, P. J., & McQueen, D. J. (1986). Internal phosphorus load in an oligotrophic Precambrian shield lake with an anoxic hypolimnion. *Canadian Journal of Fisheries and Aquatic Sciences*, *43*(3), 574–580.

Parker, J. A., Kenyon, R. V., & Troxel, D. E. (1983). Comparison of interpolating methods for image resampling. *IEEE Transactions on Medical Imaging*, *2*(1), 31–39.

Read, J. S., Hamilton, D. P., Jones, I. D., Muraoka, K., Winslow, L. A., Kroiss, R., . . . Gaiser, E. (2011). Derivation of lake mixing and stratification indices from high-resolution lake buoy data. *Environmental Modelling & Software*, *26*(11), 1325–1336.

Rueda, F. J., Sanmiguel-Rojas, E., & Hodges, B. R. (2007). Baroclinic stability for a family of two-level, semi-implicit numerical methods for the 3D shallow water equations. *International Journal for Numerical Methods in Fluids*, *54*(3), 237–268.

Rueda, F. J., & Schladow, S. G. (2003). Dynamics of large polymictic lake. II: Numerical simulations. *Journal of Hydraulic Engineering*, *129*(2), 92–101.

Shapiro, J. (1960). The cause of a metalimnetic minimum of dissolved oxygen. *Limnology and Oceanography*, *5*(2), 216–227.

Sherman, B., Bryant, L., Mobley, M., Ford, P., McGinnis, D. F., Singleton, V., . . . Little, J. C. (2012). *Review of oxygenation technologies with special reference to application in the Upper Swan Estuary*. Australia: Commonwealth Scientific and Industrial Research Organisation (CSIRO).

Singleton, V. L., Gantzer, P., & Little, J. C. (2007). Linear bubble plume model for hypolimnetic oxygenation: Full-scale validation and sensitivity analysis. *Water Resources Research*, *43*, W02405. https://doi.org/10.1029/2005WR004836

Singleton, V. L., Jacob, B., Feeney, M. T., & Little, J. C. (2013). Modeling a proposed quarry reservoir for raw water storage in Atlanta, Georgia. *Journal of Environmental Engineering*, *139*(1), 70–78.

Singleton, V. L., & Little, J. C. (2006). Designing hypolimnetic aeration and oxygenation systems—A review. *Environmental Science and Technology*, *40*(24), 7512–7520.

Singleton, V. L., Rueda, F. J., & Little, J. C. (2010). A coupled bubble plume-reservoir model for hypolimnetic oxygenation. *Water Resources Research*, *46*, W12538. https://doi.org/10.1029/2009WR009012

Smith, P. E. (2006). A semi-Implicit, three-dimensional model for estuarine circulation. *U.S. Geological Survey Open-File Report*, 2006–1004, 176.

Taylor, J. R. (1997). *An introduction to error analysis: The study of uncertainties in physical measurements*. Sausalito, CA: University Science Books.

Toffolon, M., Ragazzi, M., Righetti, M., Teodoru, C. R., Tubino, M., Defrancesco, C., & Pozzi, S. (2013). Effects of artificial hypolimnetic oxygenation in a shallow lake. Part 1: Phenomenological description and management. *Journal of Environmental Management*, *114*, 520–529.

Toffolon, M., & Serafini, M. (2013). Effects of artificial hypolimnetic oxygenation in a shallow lake. Part 2: Numerical modelling. *Journal of Environmental Management*, *114*, 530–539.

Visser, P., Ibelings, Bormans, B. M., & Huisman, J. (2016). Artificial mixing to control cyanobacterial blooms: A review. *Aquatic Ecology*, *50*, 423–441.

Wüest, A., Brooks, N. H., & Imboden, D. M. (1992). Bubble plume modeling for lake restoration. *Water Resources Research*, *28*(12), 3235–3250.